Corrosion Science 76 (2013) 27–34

Contents lists available at ScienceDirect

Corrosion Science

journal homepage: www.elsevier.com/locate/corsci

Initial stages of corrosion pits on AISI 1040 steel in sulfide solution analyzed by temporal series micrographs coupled with electrochemical techniques

Alexsandro Mendes Zimer, Matheus A.S. De Carra, Emerson Costa Rios, Ernesto Chaves Pereira, Lucia Helena Mascaro *

Laboratório Interdisciplinar de Eletroquímica e Cerâmica (LIEC), Universidade Federal de São Carlos (UFSCar), Chemistry Dept., C.P. 676, CEP 13.565-905 São Carlos, SP, Brazil

ARTICLE INFO

Article history:
Received 18 March 2013
Accepted 27 April 2013
Available online 10 May 2013

Keywords:
A. Low alloy steel
B. Electrochemical calculation
B. Polarization
C. Inclusion
C. Pitting corrosion

ABSTRACT

This work presents a study of the initial instants in the pitting corrosion of AISI 1040 steel, analyzed by temporal series micrographs coupled to an open circuit potential (E_{oc}) and polarization curves. During the E_{oc} measurement, the pit induction time and the initial pit growth in MnS inclusions was detected in alkaline sulfide solution. The pit area behavior has two distinct rate of area changes in specific regions directly associated to current slope changes. Finally, it was possible to create a three-dimensional model of the pit depth evolution on the metal, using Faraday's law and the bullet-shaped geometry.

1. Introduction

During the steel pipeline corrosion, an iron sulfide film is formed which can both inhibit or accelerate corrosion depending on the experimental conditions [1,2]. When the corrosion process is accelerated, the most aggressive corrosion form on metal surfaces is the pit corrosion [3,4]. In agreement to the literature [5,6], this corrosion occurs in specific regions such as the grain boundary, defects or MnS inclusions. In this sense, few papers use *in situ* techniques to study the pit formation [7,8], but many papers use an electrochemical approach together with *ex situ* techniques [6,9–14] to study this corrosion type. The disadvantage of this last approach is the lack of experimental information that preserves the spatial coordinates, i.e., that allows the analysis of on which point of the surface the pit starts to grow. This occurs because the current and the potential are associated with the sum of all events occurring on the surface at a given period of time [15].

In this sense, using *in situ* images of metal surface, Rybalka et al. [16], have studied pit corrosion on 20Kh13 steel and have shown that there are specific regions where pit nucleation and evolution take place. The pit nucleation and metastable growth on microelectrodes of aluminum and Fe–Al binary alloys below the pitting potential was studied by Speckert and Burstein [17]. The authors described mixed anodic/cathodic current transients due to pit nucleation, and the localized attacks are nucleated preferentially at intermetallic sites [18]. Gonsález-García et al. [19] detected these transients *in situ* by scanning electrochemical microscopy (SECM). The authors propose a mechanism to pit evolution under open circuit and potentiostatic control, and metastable pitting has been imaged for them, for the first time using SECM. Gahahari et al. [20] presents a *in situ* X-ray microtomography study of pitting corrosion in stainless steel. 3D microtomography revels how pits evolve and how the shape of pits becomes modified by MnS inclusions. Besides nucleation sites of pit formation, its number depends on many experimental factors. Rueter and Heusler [21] showed that the number of pits increases with polarization and with chloride concentration, but decreased with the increase of pH solution. It was also shown in their work that close to an active pit no other new pits were observed. The radius of the protected area for new pits increases as the concentration of chloride ions decreases and the pH solution increases [21]. In recent papers, our group, using *in situ* images, demonstrated the usefulness of following color changes on the corroding surface and associated it to sulfide films dissolution and precipitation mechanism [22]. In that paper [22], monitoring both the current and the surface image changes during a polarization experiment, we observed the influence of chloride in this type of corrosion and concluded that there is a competitive adsorption between HS^- and Cl^- species leading to a cyclic process in the sulfide film formation, as suggested in the literature [23]. In other work [24], using temporal series micrographs obtained

* Corresponding author. Tel.: +55 16 33519452; fax: +55 16 33615215.
E-mail address: lmascaro@ufscar.br (L.H. Mascaro).

0010-938X/$ - see front matter © 2013 Elsevier Ltd. All rights reserved.
http://dx.doi.org/10.1016/j.corsci.2013.04.054

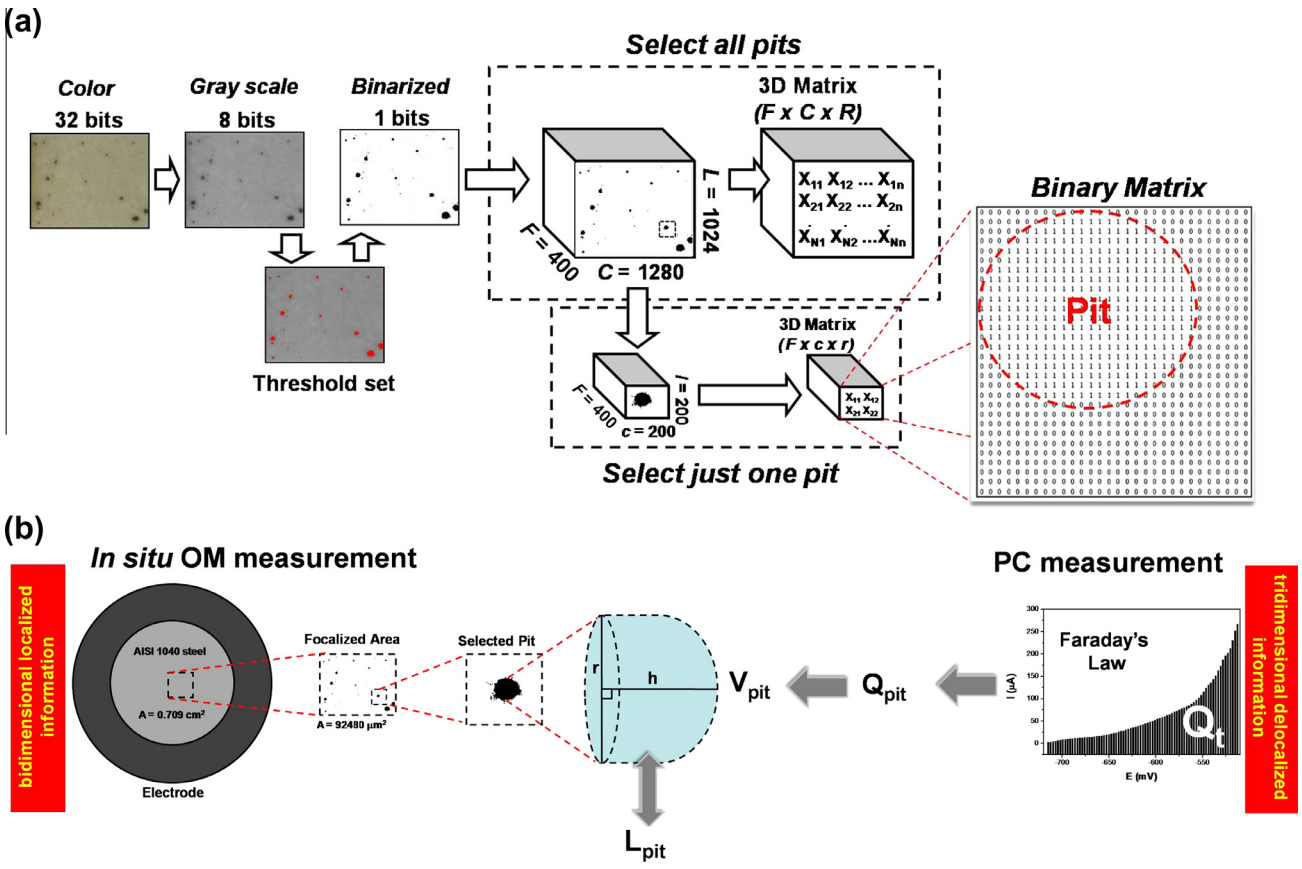

Fig. 1. Flowchart used in the digital image processing of the corroded samples using all pits and selecting just one pit (a). Bidimensional localized information of a temporal series micrograph together with a tridimensional delocalized information, from polarization curve. Fraction of Q_t to estimate the V_{pit} and the pit depth (L_{pit}) (b).

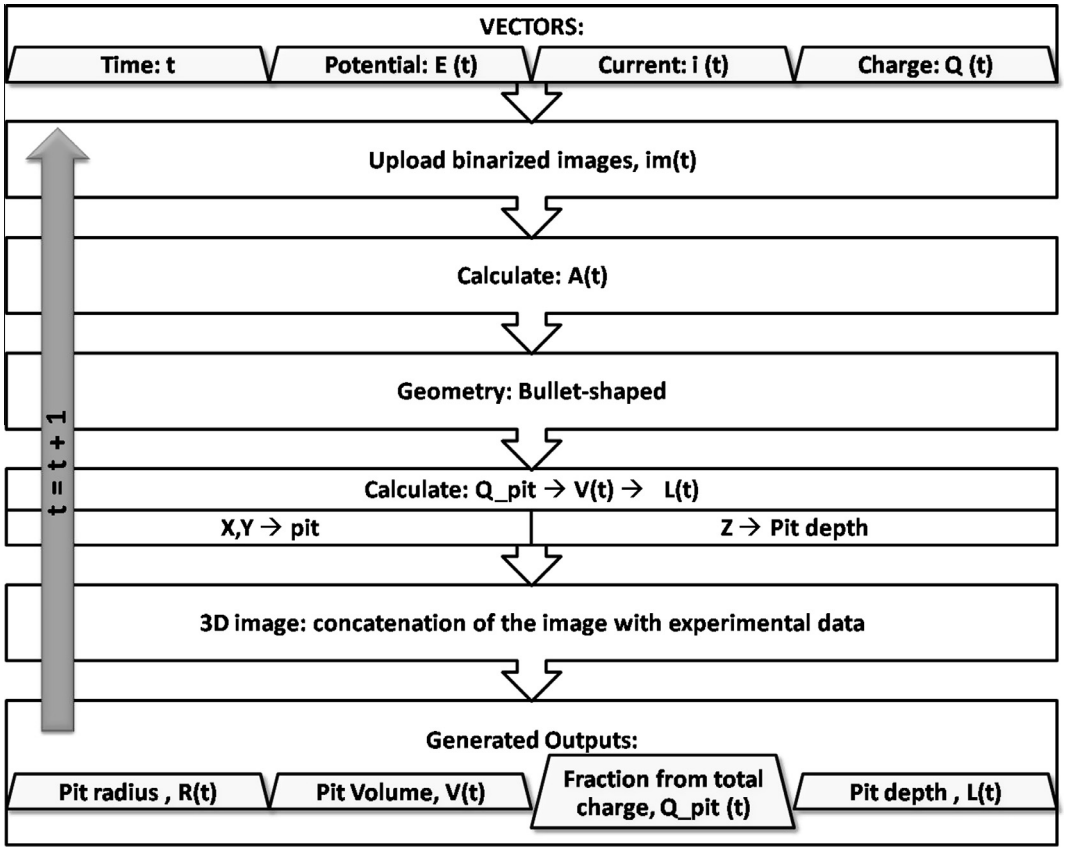

Fig. 2. Flowchart describing the algorithm employer to calculi the pit parameters.

during *in situ* experiments and Faraday's law, it was possible to estimate the mean pit depth. Thus, some processes, such as the transient nature of corrosion products [22] or even an estimation of the pit depth [24] cannot be investigated using only electrochemical methods.

The number of papers using *in situ* image acquisition during electrochemical experiments is small. In such experiments, on order to use images, first they must be converted into the appropriate coordinates. For example, to study the color texture and shape of a corrosive surface, the images can be characterized as colored (32 bits) [25], or gray scale (8 bits) [26]. If only local phenomena are studied, such as pit corrosion, binarized (1 bit) images can be used to separate the background from the object (a pit itself, in this case). Of course, the amount of information to be manipulated and, as consequence, the computational effort, decreases considerably for binarized images. In those papers, Choi and Kim [25] investigated the morphological change and classified the types of surface corrosion damage using color digital image processing, and Kapsalas et al. [26] for his turn, detected black spots in order to quantify the damages caused by corrosion.

Considering what is exposed above, this work used *in situ* optical microscopy aiming to get local information about the initial steps of pitting corrosion, during open circuit potential and polarization curve experiments, under conditions where there is sulfide film formation. This approach was applied in the investigation of pitting corrosion of AISI 1040 steel in aqueous basic solution, containing HS^- species.

2. Experimental

2.1. Preparation of electrolytic solution

A solution of 31×10^{-3} mol dm^{-3} was prepared by the dissociation of $Na_2S{\cdot}9H_2O$ (Synth) in a phosphate buffer, pH 7.9. The pH-sulfide equilibrium diagram shows that the main species presented at $5.5 < pH < 10$ is the hydrogen sulfide ion, HS^- [27].

2.2. Sample preparation

The cylindrical AISI 1040 steel (Sanchelli), with 9.5 mm diameter, was embedded in epoxy resin and used as working electrode (WE). The material composition was determined by Atomic Absorption Spectrocopy (AAS) analysis: 0.419% C, 0.703% Mn, 0.018% S, 0.007% P, 0.035% Ni, 0.132% Cu and 98.686% Fe, wt%. Prior to use, the disk electrodes ($A = 0.709$ cm^2) were abraded with sandpaper of up to 2000-grit and then polished with diamond paste of 1 and 1/4 μm, and degreased in acetone, for 3 min, in an ultrasonic bath.

2.3. Equipments

The electrode surface was observed by an inverted optical microscope (Opton – mod. TNM-07T-PL) and the images were collected using the Scope Photo® 1.0 software and MCDE (AMCAP). All electrochemical measurements were carried out using an Autolab model PGSTAT 30. An Ag/AgCl/KCl (Sat.) was used as the reference electrode (RE) and a Pt wire was used as the auxiliary electrode (AE). Two electrochemical experiments were performed. The first one was to follow the open-circuit potential (E_{oc}) during 3600 s, which is the necessary period of time for its stabilization. The second experiment was a polarization curve which started at E_{oc} and went up to a 200 mV more positive value at a scan rate of 0.1 mV s^{-1}.

2.4. Image data acquisition and quantification procedure

To perform the *in situ* image acquisition, the steel electrode was immersed in the corrosive solution in a homemade flat-bottom cell [22]. The surface electrode area of 340×272 μm^2 was recorded using an acquisition rate of 0.1 and 0.2 frame s^{-1}, during the E_{oc} and polarization curves measurements, respectively. In both cases, image data quantification was performed using the procedure described in a previous paper [24]. Fig. 1a shows the flowchart used to convert the images into information. At the end of the experiment, the binarized images, Fig. 1a, correspond to a three-dimensional matrix of $F \times C \times R$, where: F = number of frames obtained during time series micrograph ($F = \sum F_1 + F_2 + F_3 + \ldots + F_n$); C = horizontal resolution (number of columns); and R = vertical resolution (number of rows). This matrix contains all temporal information of the regions analyzed in the determined experimental conditions for multiple or single pit analysis. For the single pit analysis, a three-dimensional matrix of $F \times c \times l$ is used to select only one pit, however it keeps all temporal information of the matrix.

This matrix can be correlated to the polarization curve data in order to create a three-dimensional model of the pit depth evolution, i.e., the "bidimensional localized information" of a temporal series micrograph, from a fraction of the observed surface, together with the "tridimensional delocalized information" from the polarization curve, Fig 1b. The Faraday's law and some considerations were used to do this: (i) the current only flows through pits with a faradaic current efficiency of 100% [24]; and (ii) the current flowing through each pit is proportional to the mouth's pit area. To the three-dimensional model of the pit, the bullet-shaped geometry [28] was chosen because the pit's radii are smaller than depth

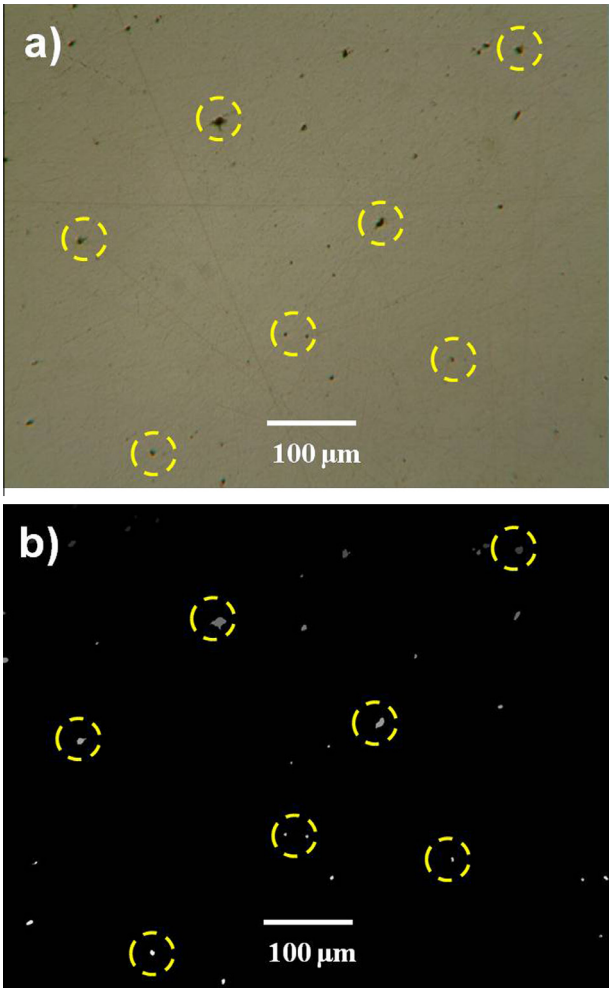

Fig. 3. Inclusion analysis of recent polished surface of AISI 1040 steel (a) binarized image to select the defects or inclusions (b). Dotted circle highlight some defects or inclusions on steel surface.

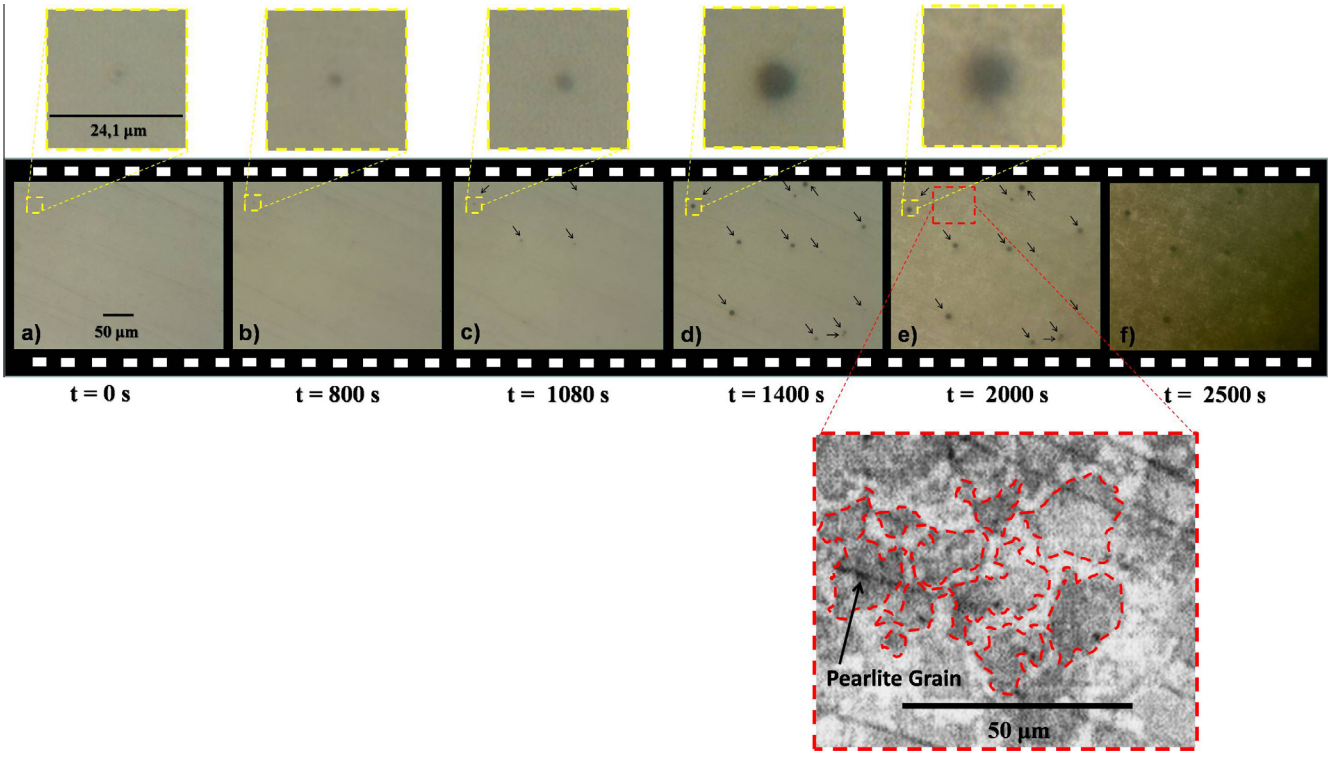

Fig. 4. *In situ* optical microscopy observation of AISI 1040 steel during the E_{oc}, in 31×10^{-3} mol dm^{-3} of HS^- species in phosphate buffer (pH 7.9) immediately after the immersion in solution (a) and in the exposition times: 800 (b), 1080 (c), 1400 (d), 2000 (e), and 2500 s (f). Dotted square indicates one defect or inclusion on steel surface and his evolution along with the grain-boundary corrosion (insets).

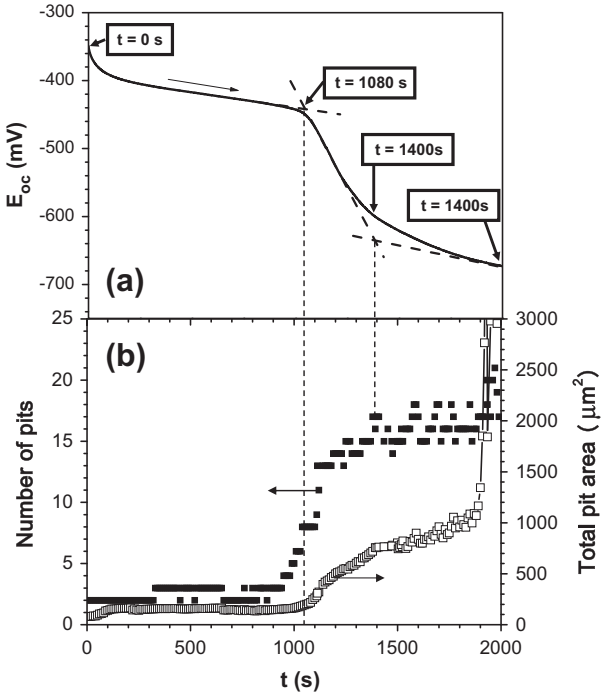

Fig. 5. E_{oc} behavior of AISI 1040 steel in 31×10^{-3} mol dm^{-3} of HS^- species in phosphate buffer (pH 7.9) (a). Total pit area, and total pit number as function of the time during E_{oc} measurement (b). E vs. Ag/AgCl/KCl.

and it is present a hemispherical bottom. For this last one, the depth (L_{pit}) was also determined by a micrometer coupled to an optical microscopy in order to compare it with the estimated pit depth.

Using the molar mass of iron (55.874 g mol^{-1}), and the AISI 1040 steel density (7.8 g cm^{-3}), the volume, in cm^{-3}, can be determined (or in pixel^3 because each pixel corresponds to 265 nm in the observed image). In the final frame (F_n), one pit is marked and its centroid is fixed to create its three-dimensional model evolution in order to predict its depth. A flowchart to describe the algorithm is presented in Fig. 2. The starting point uses data as function of the time, called vectors, from polarization curve: time, potential, current and charge. Finally, several parameters are calculated for the chosen pit: pit radius, pit volume, fraction from total charge (associated to the chosen pit), and, the most important, the pit depth at each time of the polarization measurement.

where t is the time, $E(t)$ is the applied potential, $i(t)$ is the current, $Q(t)$ is the charge, $im(t)$ is the binarized image, $A(t)$ is the area of the analyzed pit, $Q\_pit(t)$ is the associated charged with the chosen pit growth, $V(t)$ is the volume of the pit, $L(t)$ is the pit depth, and $R(t)$ is the pit radius.

3. Results and discussion

The metallographic study of AISI 1040 steel was presented in a previous work [22] and it was observed that the microstructure of the carbon steel is composed of both ferrite and pearlite grains with inclusion of MnS. The number of inclusions in the metal sample employed in this study was measured following the ASTM E 1382-97 [29]. As can be observed in Fig. 3, the number of inclusions greater than 1 µm^2 was determined as 25 ± 10 inclusion per unit of the observed area, i.e., 340×272 µm ($A_{obs} = 9.24 \times 10^4$ µm^2).

Fig. 4 shows the temporal series micrographs at open-circuit potential, E_{oc}, immersed in 3.1×10^{-3} mol dm^{-3} of HS^- at pH 7.9. As shown in the insets of Fig. 3 the pits start to grow in

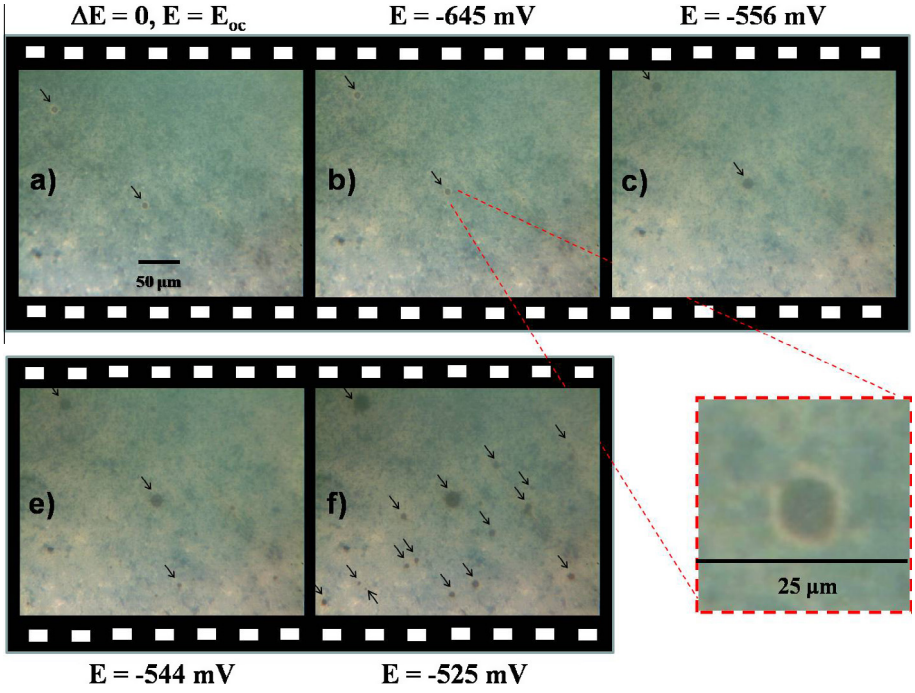

Fig. 6. *In situ* optical microscopy observation of AISI 1040 steel during the polarization curve, in 31 × 10^{-3} mol dm^{-3} of HS^- species in phosphate buffer (pH 7.9). Micrographs obtained at potential of $E = E_{oc}$ (a), and in $E = -645$ (b), −556 (c), −544 (d), −525 mV vs. Ag/AgCl/KCl (e). Dotted square focalize just one stable pit with the presence of a cathodic halo more visible in sulfide film (inset).

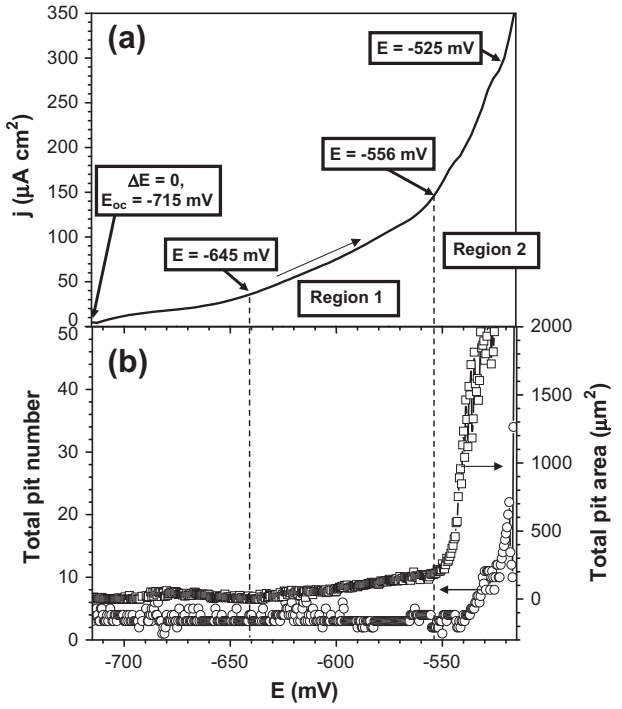

Fig. 7. Polarization curve of AISI 1040 steel in 31 × 10^{-3} mol dm^{-3} of HS^- species in phosphate buffer (pH 7.9) (a). Total pit area and total pit number as function of potential applied during polarization curve (b). *E* vs. Ag/AgCl/KCl.

the inclusions, in agreement with the literature [25,26]. In those papers [30,31], a local pH fluctuation was observed near the MnS inclusions as a result of the metastable pits initiation in these regions. For a clear visualization, one surface defect was focused on a fresh polished surface ($t = 0$ s), inset of Fig. 4a. In this inset, the localized dissolution, which characterizes the beginning of

Table 1
Rate of area change of pit in Region 1 (where the pit starts to increase in area) and Region 2 (where the pit number increases) for one selected pit in each experiment. *E* vs. Ag/AgCl/KCl.

Solutions	Measurements			
	E_{oc}/mV (*E* vs. Ag/AgCl/KCl)	Rate of area change of pit. Region 1 (μm² s^{-1})	Rate of area change of pit. Region 2 (μm² s^{-1})	Comparison between the rates[b]
[a]HS^-	715	0.20 ± 0.04	0.70 ± 0.33	3.5×

[a] 31 mol dm^{-3} of HS^- species at pH 7.9.
[b] Rate of area changes of pit: Region 2/Region 1.

the pit formation, can be observed, as well as its growth in Fig. 4b and e. It is important to emphasize that in Fig. 3, during the inclusion analysis, it was easier to detect such inclusions once there is no solution layer between the lens and the metal surface, as occurs in Fig. 4.

Observing the micrographs as the time increases, it was possible to conclude that the pit number increases between 1080 and 1400 s, Fig. 4c and d. After 1400 s the number of pits becomes constant. Punckt et al. [32], proposed that this behavior is related to the fact that there is a limited number of defects for pit nucleation on the metal surface, leading therefore to a restricted total number. Besides, in inset of Fig. 4e (2000 s), the grain boundary corrosion is revealed. This corrosion type is characterized by reveal pearlite grains (see darker grains marked with dot lines in inset of Fig. 4e) and ferrite grains (whiter grains), as showed in previous paper [22]. After this point, Fig. 4f (2500 s), a dark FeS [27] film is formed over the surface and it is no longer possible to follow pit growth. It has been proposed that pit corrosion, as the ones observed in Fig. 4, occurs due to the presence of the hydrogen sulphide ion (HS^-), which are quite aggressive and, therefore, accelerate the metal dissolution [33]. Organ et al. [34], proposed that pit formation depends on three sources: (i) aggressive ions

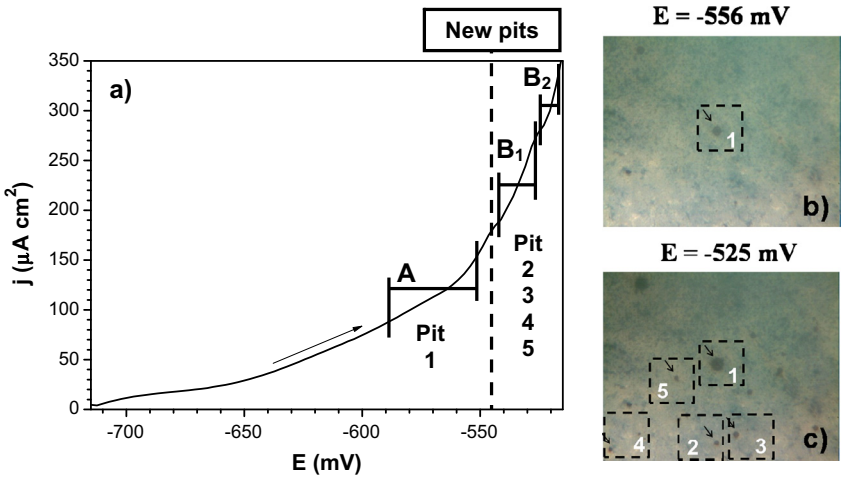

Fig. 8. *In situ* optical microscopy observation of AISI 1040 steel during the polarization curve at potential of −556 mV showing one pit (a) and in −526 mV showing new others one (b). Polarization curve showing two distinct regions, A and B, where in the first one the pit 1 were analyzing before and after the new pit events marked how 2, 3, 4, and 5 occurring (c). *E* vs. Ag/AgCl/KCl.

in the solution; (ii) defects on surface and on the passive film; and (iii) ohmic potential drop in the solution. Analyzing the E_{oc} measurement presented in Fig. 3, it is possible to observe that (i) and (ii) conditions appear on the surface during the beginning of pit corrosion and, of course, the third condition is not associated in this figure.

Another important point to highlight in Fig. 4 is that the pit ceased to grow during the E_{oc} measurement. Therefore, the pits have a maximum average size during the E_{oc} measurements. Fig. 4e shows a pit mean diameter of 6 ± 2 μm. Rybalka et al. [16] observed a maximum pit diameter of 10 μm on the 20Kh13 steel, under E_{oc} conditions, and the authors proposed that this maximum diameter is related to pit passivation. For this last one, we believed that besides the pit passivation, a redistribution of all surface sites can occur, as can be observed in Fig. 4e (see inset), when we have both the pit corrosion and the grain boundary corrosion on a metal surface.

Fig. 5 presents E_{oc} as a function of the time, as well as the quantitative image analysis of the complete time sequence presented in Fig. 4. This procedure allows us to quantify the number of pits and their total area. The initial region observed in Fig. 5a is characterized by a smooth variation in the open circuit potential value, which is known as the induction period [35]. In this step, the initial stages of pitting corrosion begun at the defects. Such behavior can be correlated with the data presented in Fig. 5b where, until 800 s, it is not possible to observe any new formed pits (see also Fig. 4a and b). After this point, in 1080 s, there is an important transition in the E_{oc} values that fall to more negative ones, which Davydov [35] classified as a typical behavior for pit corrosion. At the same time, in Fig. 5b, the pit area starts to increase continuously until 1400 s. During the E_{oc} measurement approximately 17 pits appear. This value is close to the number of inclusions, which were determined before (see Fig. 3), indicating a possible correlation between them, as suggested in the literature [27]. The number of pits with the increase of time shows a small fluctuation in their number, after 1400 s, which could be related to the noise during the binarization process. Therefore, some pits were not counted in some frames from time series micrograph during the abrupt transition of E_{oc}, leading, as consequence, to the small fluctuation in the number of pits.

The slope in the total pit area vs. time plot of Fig. 5 can be used to calculate the pit area growth rate, where two different rates were detected. The first one, between 1080 and 1400 s is of 1.3 $\mu m^2 s^{-1}$, and the second one, in the range from 1400 s until 1800 s, is of 0.62 $\mu m^2 s^{-1}$. The reduction in pit growth rate can be related to pit passivation [16] and to the redistribution of all corrosion sites during the initial grain-boundary corrosion. From a different point of view, the pit growth rate can be reduced due to the increase on the quantity of pits in the first region, which remain constant in the second one. An inflection point during the accentuated fall of E_{oc} can also be observed in Fig. 5a, which occurs at 1400 s and is possibly associated to the change in the pit growth behavior described above.

Finally, after 2000 s, as shown in Fig. 5b, it was not possible to follow the occurrence of pit numbers since there is a dark sulfide film growing on the metal surface (see Fig. 4f) and it causes an abrupt increment in the total pit area. The E_{oc} decrease is also an indication of the passivation process, since it is associated with a large amount of Fe^{2+} dissolved into the solution, which favors the FeS formation, as confirmed by EDS measurements (results not shown).

In a second set of experiments, the electrodes were evaluated during the polarization curve and the results are presented in Fig. 6.

As can be observed in Fig. 6, when the applied potential is displaced to positive values, the quantity of pits begin to rise. The inset of Fig. 6 shows an active pit and its cathodic halo during its polarization. Fig. 7 quantifies the data presented in Fig. 6. The polarization curve is shown in Fig. 7a and the total pit area and the number of pits is presented in Fig. 7b, as a function of the applied potential. The total pit area curve reveals the presence of two regions. Vertical lines mark the limit of these regions. In the first

Table 2
Individual rate of area changes of five pits in different potential regions during the polarization curve of Fig. 6. *E* vs. Ag/AgCl/KCl.

Pits	Rate of area changes of pits ($\mu m^2 s^{-1}$)		
	Region A (−587 to −548 mV) *E* vs. Ag/AgCl/KCl	Region B_1 (−542 to −526 mV) *E* vs. Ag/AgCl/KCl	Region B_2 (−526 to −518 mV) *E* vs. Ag/AgCl/KCl
1	0.172 ± 0.05	0.44 ± 0.19	1.5 ± 0.58
2	–	0.14 ± 0.05	0.38 ± 0.16
3	–	0.10 ± 0.16	0.48 ± 0.31
4	–	0.12 ± 0.05	0.31 ± 0.09
5	–	0.14 ± 0.05	0.46 ± 0.28

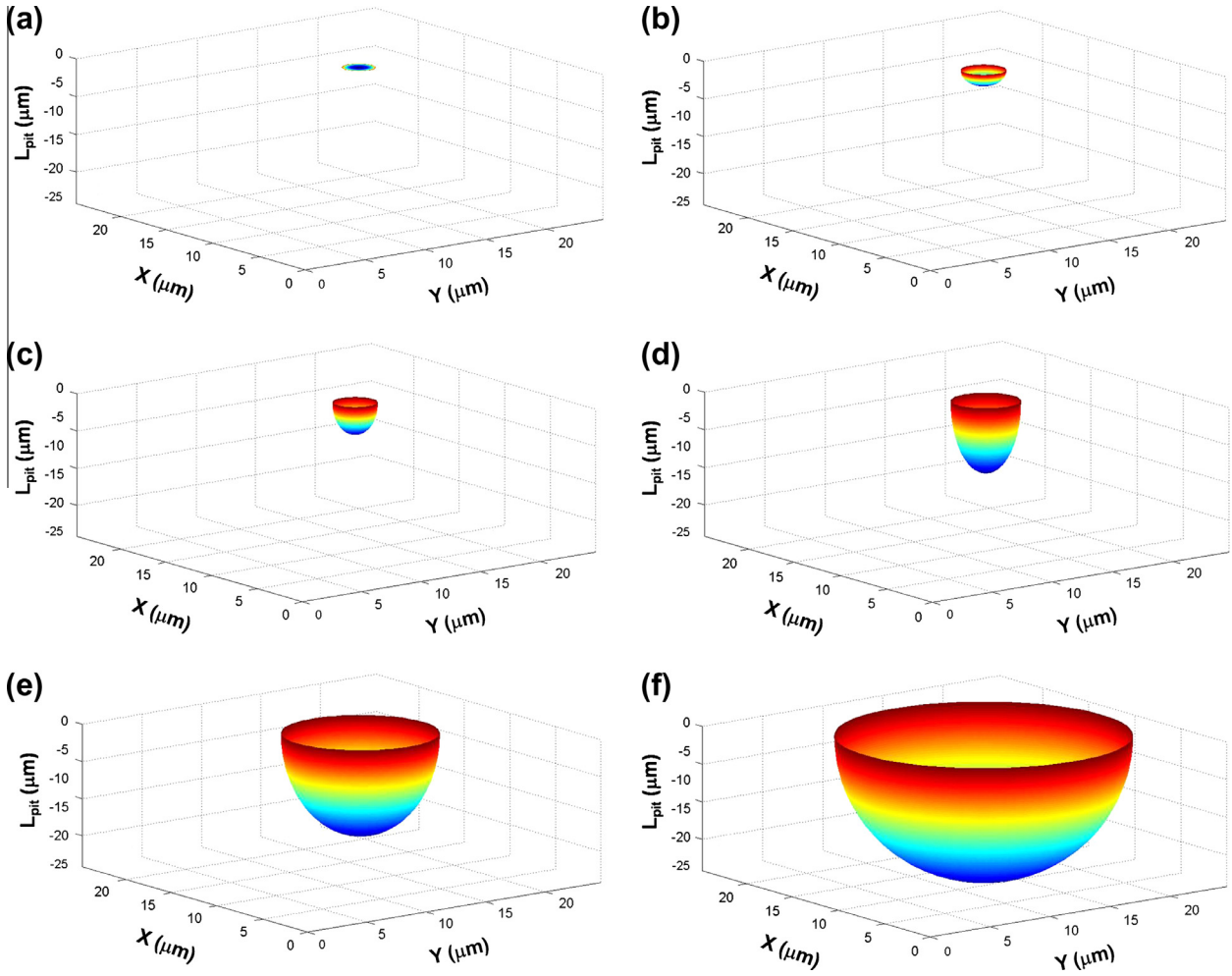

Fig. 9. Three dimensional model using a bullet-shaped geometry to a single pit to estimate the pit depth (L_{pit}) as function applied potential showing his evolution: $E = E_{oc}$ (a), −625 (b), −585 (c), −550 (d), −535 (e), and −521 mV (f). E vs. Ag/AgCl/KCl.

one, only the pit areas increase and in the second region both the pit number and pit area increases. In this last region we also have a higher pit area increment.

From the slopes of the total pit area plot (Fig. 7b) it is possible to calculate the pit evolution rates, in the first and second regions. The second rate is higher than the first one, but occurs in the same region where an explosion in the number of pits is observed, Fig. 7b. Then, in fact, the second rate could be related to new pits, which are formed in this region and therefore contribute more expressively to the corrosion process. To remove this doubt, a single pit was selected (see centric pit of Fig. 6, detached at inset) and the pit evolution rate were calculated in these two regions, see Table 1 to HS^- solution. The second rate in Table 1 is higher than the first one by 3.5 times, corroborating with this proposition (Fig. 7b). Therefore, one possible explanation for the pit rate increase in the second region is related to the reached critical potential, i.e. the E_{pit}, where new pits are formed.

In a previous published paper [24], our group performed also experiments in 31×10^{-3} mol dm^{-3} of HS^- species in phosphate buffer (pH 7.9), but in the presence of Cl^- ions (3.5 wt.% or 0.6 mol dm^{-3}). The same behavior presented in Fig. 7 was found for those experimental conditions. In that case, the second rate of area change of pit that occurs in the region of the new growing pits is 27 times higher than in the first one. Therefore, that result could mean that the corrosion pits in the chloride solution depassivate the surface, and, therefore make it more dangerous to mechanically stabilize the material. This proposition is also supported the data collected by Veloz and Gonsález data [23], which proposes that the Cl^- ions are able to prevent the formation of sulfide films due to their competitive adsorption with the HS^- ions.

To characterize this last experimental fact, analysis of the growth behavior for the 5 different pits were carried out using the data presented in Fig. 6, and they are shown in Fig. 8. In this Figure, the dotted line shows when a new pit arise.

In Fig. 8a, a vertical line in −545 mV vs. Ag/AgCl/KCl shows that after this point new pits start to appear on the metal surface. Fig. 8b (at −556 mV) and Fig. 8c (at −525 mV vs. Ag/AgCl/KCl) shows micrographs retired respectively before and after this vertical line. This first potential range was called region "A", and the second one as region "B". The more positively potential region is then subdivided into two new regions, "B_1" and "B_2". Such choice was necessary since potentials higher than −525 mV vs. Ag/AgCl/KCl have accelerated the rate of area changes of pit. Only pit number 1 is observed in all regions, therefore, it is the only contribution to Region A (Table 2). The results are summarized in Table 2.

The pits which arise (appear) in region B (2, 3, 4, and 5), have approximately the same rates of area changes of pit, being of 0.13 μm^2 s^{-1} and 0.4 μm^2 s^{-1}, in region B_1 and B_2, respectively. This means that they grow at the same rate, and therefore the changes in pit growth rates have the same value for all new pits investigated. With this information it is possible to build a three dimensional model to estimate the pit depth and then apply it to a single pit as a representation of all the pits.

In an earlier paper [24], the normalized charge for the total pit area occupied in the observed area was used to predict the mean of the pit depth of all the pits during the *in situ* experiment. In the present case, we present the growth of only one pit, using a tridimensional representation based on Faraday's law, supposing that the fraction of the total dissolution current associated with the chosen pit area. With the experimental approach here developed it is possible to estimate the growth of a pit during a polarization curve measurement. To estimate the pit depth, it is necessary to propose a given geometry for this pit. It is known that a pit can have various geometries, such as: hemispherical, saucer-like (shallow disk), flat-walled, polished, etched, covered or uncovered pits [36], and bullet-shaped ("U-shape") [28]. The allocation of the hemispherical pit geometry has been widely used in the literature for many years [9,16,28,36–39]. The pit's geometry depends on the aggressiveness of the solution and the nucleation sites. This last one depends on the metal or alloy composition [36]. In the present work, it was observed by *ex situ* optical microscopy that the pits in sulfide solution have geometry close to bullet-shaped, where the pit's radii are smaller than depth during the pit growth, and an external cathodic halo (see inset of Fig. 6). Therefore, the pit's estimated depth is based on the bullet-shaped geometry and a fraction of the total charge (Q_t) were used to estimate the pit volume (V_{pit}) using this geometry.

Fig. 9 shows the growth of pit 1 during the polarization curve measurement of Fig. 7a (also see inset of Fig. 8a). In this Figure, a three-dimensional model of the surface shows the evolution of the pit at different potential values in order to estimate the pit depth, Fig. 9a–f. The pit observed in Fig. 9 has a maximum depth of 25 μm until the end of the anodic polarization measurement (200 mV more positive than the E_{oc}). To confirm this value, a micrometer was coupled to the optical microscope, and then it was possible to measure the pit depth, which is, in this case, close to 20 ± 10 μm which indicates a good correlation between the optical measurements and its estimative.

In summary, using bidimensional localized information of a temporal series micrograph, from a fraction of the observed surface, together with tridimensional delocalized information from the polarization curve, it was possible to associate a fraction of this total current to the amount of dissolved iron ions that was loosened during the corrosion process. This approach allows us to estimate the progress of pitting corrosion on metallic materials, in agreement to Faraday's law.

4. Conclusions

The method presented here described the study of localized corrosion in real time conditions, using temporal series micrographs coupled to electrochemical techniques. The initial stages of corrosion pitting, such as the induction time and growth, were detected and quantified. The E_{oc} measurement presents an accentuated decrease towards more negative values, while simultaneously, the quantity of pits and its area increases. During the polarization curves measurements, two distinct regions were observed. During the first one, a total pit area change is observed without any increase in their number. In the second one, news pits appear in regions adjacent to the stable pits earlier detected. It is interesting to observe that all the investigated pits grow with approximately the same rate in both regions. Finally, based on the normalized charge of one of the pits, and using Faraday's law, it was possible to propose a three-dimensional model to follow the pit growth. From this model, the pit depth can be estimated. Therefore, the approach used here allowed us to use 2D localized information (micrographs) with non localized 3D information (current during a polarization curve experiment), in order to follow the corrosion process with a 3D localized method.

References

[1] H. Ma, X. Cheng, G. Li, S. Chen, Z. Quan, S. Zhao, L. Niu, Corros. Sci. 42 (2000) 1669–1683.
[2] L.L. Shreir, Corrosion Of Metals And Alloys, I, Wiley-Interscience, New York, 1978.
[3] C. Ren, D. Liu, Z. Bai, T. Li, Mater. Chem. Phys. 93 (2005) 305–309.
[4] C.R.F. Azevedo, Eng. Fail. Anal. 14 (2007) 978–994.
[5] Y. Li, R. Hu, J. Wang, Y. Huang, C. Lin, Electrochim. Acta 54 (2009) 7134–7140.
[6] H.C. Man, D.R. Gabe, Corros. Sci. 21 (1981) 713–721.
[7] M. Reffass, R. Sabot, M. Jeannin, C. Berziou, P. Refait, Electrochim. Acta 54 (2009) 4389–4396.
[8] J. Li, D. Lampner, Colloid Surf. A 154 (1999) 227–237.
[9] M.A. Amin, S.S. Abd El Rehim, A.S. El-Lithy, Corros. Sci. 52 (2010) 3099–3108.
[10] T. Henriques, A. Reguengos, L. Proença, E.V. Pereira, M.M.M. Rocha, M.M. Neto, I.T.E. Fonseca, J. Appl. Electrochem. 40 (2009) 99–107.
[11] M.A. Amin, Electrochim. Acta 50 (2005) 1265–1274.
[12] H.H. Hassan, Electrochim. Acta 51 (2005) 526–535.
[13] Y.F. Cheng, J.L. Luo, Electrochim. Acta 44 (1999) 4795–4804.
[14] A. Gebert, F. Schneider, K. Mummert, Nucl. Eng. Des. 174 (1997) 327–334.
[15] G.S. Frankel, J. Electrochem. Soc. 145 (1998) 2186–2198.
[16] K.V. Rybalka, L.A. Beketaeva, V.S. Shaldaev, L.V. Kasparova, A.D. Davydov, Russ. J. Electrochem. 45 (2009) 1217–1225.
[17] L. Speckert, G.T. Burstein, Corros. Sci. 53 (2011) 534–539.
[18] R. Ambat, A.J. Davenport, G.M. Scamans, A. Afseth, Corros. Sci. 48 (2006) 3455–3471.
[19] Y. González-García, G.T. Burstein, S. González, R.M. Souto, Electrochem. Commun. 6 (2004) 637–642.
[20] S.M. Ghahari, A.J. Davenport, T. Rayment, T. Suter, J. Tinnes, C. Padovani, J.A. Hammons, M. Stampanoni, F. Marone, R. Mokso, Corros. Sci. 53 (2011) 2684–2687.
[21] M. Reuter, K.E. Heusler, Electrochim. Acta 35 (1990) 1809–1814.
[22] A.M. Zimer, E.C. Rios, P.C.D. Mendes, W.N. Gonçalves, O.M. Bruno, E.C. Pereira, L.H. Mascaro, Corros. Sci. 53 (2011) 3193–3201.
[23] M.A. Veloz, I. Gonzalez, Electrochim. Acta 48 (2002) 135–144.
[24] A.M. Zimer, E.C. Rios, L.H. Mascaro, E.C. Pereira, Electrochem. Commum. 13 (2011) 1484–1487.
[25] K.Y. Choi, S.S. Kim, Corros. Sci. 47 (2005) 1–15.
[26] P. Kapsalas, M. Zervakis, P. Maravelaki-Kalaitzaki, Corros. Sci. 49 (2007) 4415–4442.
[27] M. Pourbaix, Atlas Of Electrochemical Equilibria In Aqueous Solution, second ed., NACE International, Houston, 1974.
[28] A. Turnbull, D.A. Horner, B.J. Connolly, Eng. Fract. Mech. 76 (2009) 633–640.
[29] ASTM E 1382-97, NTU, 1997, pp. 855–878.
[30] J.O. Park, M. Verhoff, R. Alkire, Electrochim. Acta 42 (1997) 3281–3291.
[31] H. Böhni, T. Suter, A. Schreyer, Electrochim. Acta 40 (1995) 1361–1368.
[32] C. Punckt, M. Bölscher, H.H. Rotermund, A.S. Mikhailov, L. Organ, N. Budiansky, J.R. Scully, J.L. Hudson, Science 305 (2004) 1133–1136.
[33] E.B. Hansson, M.S. Odziemkowski, R.W. Gillham, Corros. Sci. 48 (2006) 3767–3783.
[34] L. Organ, Y. Tiwary, J.R. Scully, A.S. Mikhailov, J.L. Hudson, Electrochim. Acta 52 (2007) 6784–6792.
[35] A.D. Davydov, Russ. J. Electrochem. 44 (2007) 835–839.
[36] R.C. Alkire, K.P. Wong, Corros. Sci. 28 (1988) 411–421.
[37] D.A. Horner, B.J. Connolly, S. Zhou, L. Crocker, A. Turnbull, Corros. Sci. 53 (2011) 3466–3485.
[38] D. Rivas, F. Caleyo, A. Valor, J.M. Hallen, Corros. Sci. 50 (2008) 3193–3204.
[39] P.C. Pistorius, G.T. Burstein, Corrosion 33 (1992) 1885–1897.